



# Drag reduction mechanisms of a car model at moderate yaw by bi-frequency forcing

Ruiying Li, Jacques Borée, Bernd R. Noack, Laurent Cordier, Fabien Harambat

## ► To cite this version:

Ruiying Li, Jacques Borée, Bernd R. Noack, Laurent Cordier, Fabien Harambat. Drag reduction mechanisms of a car model at moderate yaw by bi-frequency forcing. *Physical Review Fluids*, 2019, 4 (3), 10.1103/PhysRevFluids.4.034604 . hal-03088610

**HAL Id: hal-03088610**

**<https://hal.science/hal-03088610>**

Submitted on 20 Nov 2022

**HAL** is a multi-disciplinary open access archive for the deposit and dissemination of scientific research documents, whether they are published or not. The documents may come from teaching and research institutions in France or abroad, or from public or private research centers.

L'archive ouverte pluridisciplinaire **HAL**, est destinée au dépôt et à la diffusion de documents scientifiques de niveau recherche, publiés ou non, émanant des établissements d'enseignement et de recherche français ou étrangers, des laboratoires publics ou privés.

## Drag reduction mechanisms of a car model at moderate yaw by bi-frequency forcing

Ruiying Li,<sup>1,\*</sup> Jacques Borée,<sup>1</sup> Bernd R. Noack,<sup>2,3,4,5</sup> Laurent Cordier,<sup>1</sup> and Fabien Harambat<sup>6</sup>

<sup>1</sup>*Institut Pprime, CNRS – Université de Poitiers – ISAE-ENSMA, 86360 Futuroscope Chasseneuil, France*

<sup>2</sup>*LIMSI-CNRS, UPR 3251, 91405 Orsay Cedex, France*

<sup>3</sup>*Technische Universität Braunschweig, 38106 Braunschweig, Germany*

<sup>4</sup>*Technische Universität Berlin, 10623 Berlin, Germany*

<sup>5</sup>*Harbin Institute of Technology, Graduate School Shenzhen, 518058 Shenzhen, China*

<sup>6</sup>*PSA Groupe, Centre Technique de Vélizy, 78140 Vélizy-Villacoublay, France*



(Received 28 June 2018; published 19 March 2019)

A bi-frequency open-loop control strategy aiming to combine both high- and low-frequency forcing effects is used to experimentally reduce the drag of a simplified car model at a slight yaw angle of  $5^\circ$ . The unforced mean wake features a lateral asymmetry which induces a low base pressure footprint close to the leeward side and increases drag compared to the aligned model. Forcing is performed with pulsed jets along the windward trailing edge. High-frequency forcing acts as a time-invariant flap. The fluidic flap effect deviates the windward shear layer towards the leeward side and reduces the wake bluffness, but the lateral asymmetry of the near wake is still observed. The drag reduction related to this high-frequency forcing is about 6% with a high actuation efficiency. A modulation of the high-frequency forcing with a low-frequency component is then introduced in order to modify the mass and momentum exchange in the separating shear layer at the windward trailing edge. We find that the modulated forcing provides the ability to manipulate the mean wake orientation while maintaining the fluidic flap effect. Among all wake orientations, those reducing drag are the ones having a mean symmetric wake. The bi-frequency control strategy leads to a maximum drag reduction of 7% for the best choice of frequencies. Importantly, the bi-frequency control is more efficient than the single high-frequency forcing, the actuator requiring only half the actuation energy and presenting an actuation efficiency multiplied by 3. Finally, the physical mechanisms related to drag reduction are carefully analyzed. In particular, we show that the wake symmetrization reduces the global production of turbulent kinetic energy in the shear layers. These results open up opportunities for closed-loop control of wake asymmetries.

DOI: [10.1103/PhysRevFluids.4.034604](https://doi.org/10.1103/PhysRevFluids.4.034604)

### I. INTRODUCTION

Road vehicles are often exposed to side flows, for example when passing through a constant crosswind, wind gusts, or unsteady wakes brought by other vehicles. In these cases, aerodynamic yaw angles are imposed on the vehicle and yield asymmetric pressure distribution over the side surfaces of the vehicle. Such asymmetric features induce an imbalance of aerodynamic forces acting on the vehicle and raise mainly two concerns. First, the driving comfort and safety, especially under unsteady crosswinds, may be affected. The vehicle can be deviated from its trajectory by the combined action of the side force and yaw moment. In the cases of buses, trucks, or trains,

\*ruiying.li@ensma.fr

the vehicle can be even overturned by the effect of roll moment [1] due to their large lateral side area. These phenomena are mostly the concerns for large yaw angles of more than 20 degrees or for strongly unsteady crosswinds. Second, the drag increases under crosswind conditions as observed in previous studies [2–6]. References [2] and [6] reported a quasilinear drag increase with increasing yaw angles up to  $15^\circ$ . This increased drag is of major interest especially at small yaw angles, as the yaw moment barely induces any safety risk in this case. Small angles commonly appear in the real world situations. Reference [7] shows that the majority of possible yaw angles are within the range of  $0^\circ$  to  $6^\circ$ , which covers more than 88% of the probability distribution. Hence, drag reduction at small yaw angles is of great importance for car manufacturers.

This study will not consider the driving safety due to large yaw angles or strongly unsteady crosswinds, because the Ahmed model geometry used in this work is not a good candidate for such cases. The focus of this paper is to understand how a near wake of vehicles at small yaw angles can be modified by fluidic forcing and its influence on drag. The simplest strategy is to investigate the wake at a representative average yaw angle [8]. Although the aerodynamics under steady yaw conditions differs significantly from unsteady crosswind flows, the findings from the simplified steady configuration provide insights to the research on more complicated oncoming flow dynamics.

Flow control, a rapidly progressing research field [9,10], can be exploited for the wake manipulation. Although a lot of studies have been performed for vehicles at zero yaw angle [11–14], flow control on yawed configurations is still rare. Reference [5] minimizes the drag force of a subscaled Ahmed body with two lateral rear flaps. Optimal flap configurations, which are nonsymmetric for nonzero yaw angles, minimize the lateral force on the vehicle, while also minimizing the contribution of the flap-induced drag. Based on their results, an adaptive flap system can be designed to improve the static-flap performance. Active flow control with a steady Coandă blowing was investigated in [15] and [16]. The authors developed a robust multivariable closed-loop control strategy from experimental data. The controller reduces the yaw moment to zero at a yaw angle as large as  $10^\circ$ , whereas the drag is slightly increased compared to the unforced flow. However, the physical mechanisms by which the forced wake modifies the aerodynamic forces remain to be clarified in both [5] and [15].

The studies above directly impact the geometry of the model by the addition of base flaps or curved surfaces. On one hand, such add-on devices may be impractical and limited by the design. On the other hand, the steady blowing requires a high energy investment. To improve the practical applicability and actuation efficiency, the use of unsteady blowing such as synthetic or pulsed jets is a promising alternative strategy [17]. According to the studies of [18], unsteady blowing along the trailing edges of a square-back car model using pulsed jets can produce similar aerodynamic performance as the flaps. Yet, it affects directly the wake dynamics without changing the model geometry. This is a great advantage over passive devices. In addition, the interaction of the unsteady jets at distinct frequencies with the unstable wake dynamics constitutes a key enabler for flow control. Low-frequency forcing amplifies the development of shear layers and thus modifies the large-scale coherent structure in the wake. It has been demonstrated to either enhance the flow global instability manifested by the amplified oscillation of vortex shedding [19–21] or attenuate the instability by mitigating the formation of shedding [22]. In contrast, the high-frequency forcing is shown to create a fluidic flap effect and stabilize the turbulent wake fluctuations [18,19,23–25]. Recently, the effect of a high-frequency synthetic jet was studied numerically by [26] on a simplified oscillating truck cabin. This action was shown to be beneficial for the drag reduction and flow stabilization.

As far as we know, there is no previous experimental work in which pulsed jets have been used for the control of road vehicles at yawed conditions. The present work aims to explore this promising field and brings out novel ways to manipulate the wake. For that, we apply pulsed jets along the lateral trailing edges of a square-back car model subjected to a moderate yaw angle of  $5^\circ$ . This situation is considered as a representative problem in real life since small yaw angles have a high probability of occurrence [7]. Our goal is to identify the forcing effects on wake and drag as well as to clarify the physical mechanisms.

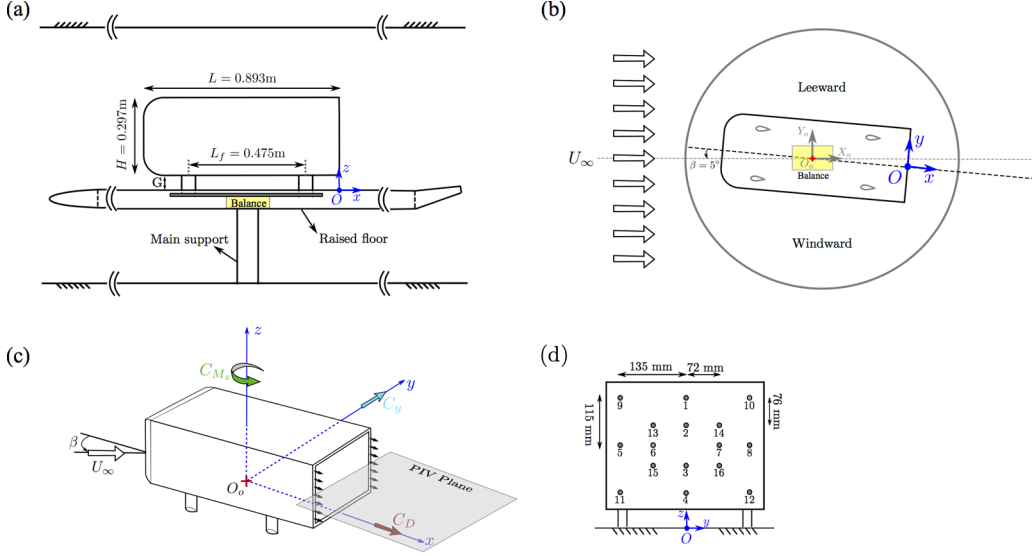


FIG. 1. Sketch of the yawed model setup. (a) Wind tunnel and model geometries. (b) Top view of the yawed model. (c) Perspective view. (d) Locations of the pressure sensors over the base surface.

The paper is organized as follows. In Sec. II, we describe the experimental setup of the square-back car model and the measurement facilities. We present the unforced baseline flow and the fluidic flap effect related to the high-frequency forcing in Sec. III. Section IV proposes a novel actuation strategy which modulates the high-frequency signal with the low-frequency signal [27]. This modulated actuation provides a control of the mean wake orientation. The wake properties for relevant forcing frequencies are also discussed. Section V concludes with a summary and outlook.

## II. EXPERIMENTAL SETUP

### A. Model positioning in the wind tunnel

The experiments were conducted in a closed-loop wind tunnel. The test section is 2.4 m wide, 2.6 m high, and 6 m long. The positioning of the blunt-edged car model in the test section is presented in Fig. 1(a) from a side view and in Fig. 1(b) from a top view. The model is similar to the square-back Ahmed body [28] but presents a slightly different geometry. The height, width and length of the model are  $H = 0.297$  m,  $W = 0.350$  m, and  $L = 0.893$  m, respectively. The front edges are rounded with a radius of 0.085 m. We mount the model over a raised floor with an elliptical leading edge to control the boundary layer thickness, which is  $\delta_{0.99} = 0.04H$  when measured at the location of the front surface of the model. The corresponding shape factor is  $H_{\text{shape}} = 1.4$ , suggesting a turbulent boundary layer. The ground clearance is set at  $G = 0.05$  m  $= 0.17H$ , which is about  $4\delta_{0.99}$ . A trailing-edge flap at the end of the raised floor is carefully regulated to ensure a zero incident angle on the leading edge with the presence of model.

Two coordinate systems are distinguished: the aerodynamic coordinates  $(X_o, Y_o, Z_o)$  with  $X_o$  parallel to the free-stream velocity  $U_\infty$  and the body-fixed coordinates  $(x, y, z)$  aligned with the length axis of the car model. The origin of the former system lies at point  $O_o$  which is located on the raised floor and at the center of the car model, while the origin  $O$  of the latter system is placed on the raised floor at the streamwise position of the rear surface for a clear description of the wake region. Crosswind is simulated by turning the model with respect to the upstream velocity by a yaw angle  $\beta$  [see Fig. 1(b)]. Here the yaw angle is fixed at  $\beta = 5^\circ$ . The lateral side which is sheltered from the wind is called leeward, while the opposite side facing the wind is denominated as windward. The experiments were performed at  $U_\infty = 25$  m s<sup>-1</sup>, corresponding to a Reynolds

TABLE I. Tested periodic forcing parameters.  $N_s$  is the number of sampling points in one time period of  $f \in [0, 500]$  Hz.

| $N_s$ | $f$ (Hz) | $St_H$ | DC  | $N_s$ | $f$ (Hz) | $St_H$ | DC  |
|-------|----------|--------|-----|-------|----------|--------|-----|
| 500   | 10       | 0.12   | 47% | 74    | 68       | 0.8    | 46% |
| 357   | 14       | 0.17   | 47% | 63    | 80       | 1      | 46% |
| 278   | 18       | 0.21   | 47% | 50    | 100      | 1.2    | 48% |
| 250   | 20       | 0.24   | 47% | 33    | 151      | 1.8    | 45% |
| 156   | 32       | 0.38   | 47% | 25    | 200      | 2.4    | 48% |
| 125   | 40       | 0.48   | 47% | 20    | 250      | 3      | 45% |
| 100   | 50       | 0.6    | 47% | 10    | 500      | 6      | 40% |

number  $Re_H \approx 5 \times 10^5$ , based on the height  $H$  of the model. The oncoming velocity is not regulated during the experiments. Its standard deviation is about 0.4% of the oncoming flow.

### B. Pulsed jet actuator

The model is equipped with four independent actuator slits along the trailing edges. The slit width is 1 mm. In this study, only the lateral slits are used for actuation. Pulsed jets are blown tangentially to the axis  $x$  through these slits, as shown in Fig. 1(c). The pulsed blowing is driven by solenoid valves working in on/off mode within the frequency range  $f \in [0, 500]$  Hz. The corresponding Strouhal number range is  $St_H = fH/U_\infty \in [0, 6]$ . The actuation amplitude can be modified by changing the supply pressure in the compressed air reservoir located inside the model. In this study, we apply a proportional-integral-derivative (PID) controller to maintain the reservoir pressure at  $P_0 = 2.5$  bar during the actuation for all investigated frequencies.

The actuation command  $b$  is generated by a National Instrument PXIe-8820 Real-Time controller running at a sampling rate of  $F_s = 5$  kHz [29]. The solenoid valves imply that  $b$  is binary, the valves being closed at  $b = 0$  and opened at  $b = 1$ . This binary command is obtained by calculating  $b(t) = H(\sin(2\pi ft) - 0.1)$  where  $H$  is the Heaviside function, i.e.,  $H(x) = 0$  if  $x \leq 0$ ,  $H(x) = 1$  otherwise. The periodic forcing frequency  $f$  is determined by  $f = F_s/N_s$ , where  $N_s$  is the number of sampling points in one time period of  $f$ . The constant value  $-0.1$  is chosen to impose a duty cycle slightly smaller than 50%. The reason is twofold, based on the studies of [30]. First, duty cycles larger than 50% perform worse than small ones in terms of drag reduction. Second, duty cycles smaller than 40% pose a problem for the functionality of the solenoid valves for high-frequency forcing. The tested frequencies  $f$  and duty cycles DC in the present study are shown in Table I. The jet velocity  $V_{jet}$  was measured at 1 mm downstream the centerline of the slit exit by use of a single hot-wire probe in still air. We display in Fig. 2(a) the time series of  $V_{jet}$  at two frequencies,

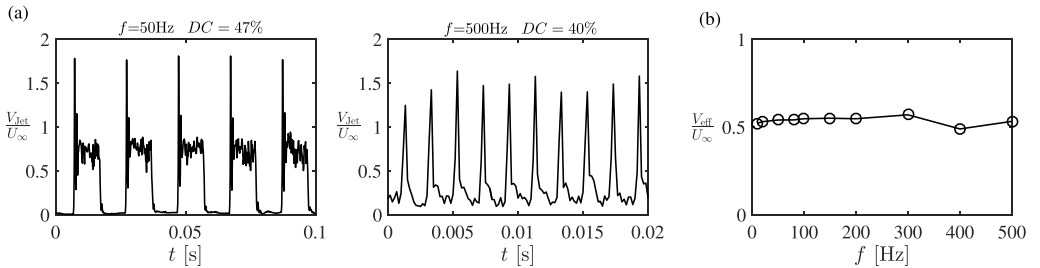


FIG. 2. (a) Time series of the jet velocity at  $f = 50$  and 500 Hz. (b) The evolution of the effective jet velocity as a function of the frequency.

$f = 20$  and  $500$  Hz. At  $f = 20$  Hz, the velocity signal presents a rectangular waveform with an overshoot at the beginning of each stroke phase, while at  $f = 500$  Hz the signal presents an irregular triangle waveform. The actuation amplitude is quantified by the effective jet velocity  $V_{\text{eff}}$ , defined as  $V_{\text{eff}} = (\overline{V_{\text{jet}}^2})^{\frac{1}{2}}$ , where the overline denotes the time average. Figure 2(b) shows the evolution of  $V_{\text{eff}}$  as a function of the frequency  $f$  under constant supply pressure ( $P_0 = 2.5$  bar). For all the considered frequencies, we have  $V_{\text{eff}} \approx 0.5U_{\infty}$ . For more information on the actuator system, see [30].

### C. Measurements of forces and moments

A six-component force and moment balance was used to measure the forces and moments acting on the model along the three directions. The measuring system is composed of a 9129AA Kistler multicomponent dynamometer using piezoelectric force sensors and a 5080A charge amplifier. The calibrated range used is  $[0, 60]$  N. The repeatability of the force measurements has been checked both in and out of the wind tunnel. Note that the nonlinearity due to the interactions among different components (systematic errors) are calibrated and the signal drift related to the piezoelectric sensors are corrected, both ensuring the accuracy of the measurements. For details, see [29].

As shown in Fig. 1(a), the balance is mounted inside the raised floor and is connected to the model with a metal plate of thickness 15 mm. The metal plate is connected to the model by the use of four profiled supports and is aligned with the model, while the balance is parallel to the wind tunnel axis  $X_o$ , as depicted in Fig. 1(b). Thus the balance measures aerodynamic forces in the wind tunnel frame. However, we are interested in the forces in the model frame as the drag to be overcome by the propulsion system is against the car's travel motion. The measured quantities are thus projected on the body axes  $(x, y, z)$  with the origin  $O_o$  of the wind tunnel frame, as presented in Fig. 1(c). The data are acquired for at least 50 s by a 16-channel Data Translation DT9857E data acquisition module at 100 Hz. A low-pass filter at 10 Hz is used to get the time-averaged forces  $F_i$  and moments  $M_i$  with  $i \in \{x, y, z\}$ .

In this paper, we focus on the control effects on the drag  $F_D$ . The corresponding drag coefficient  $C_D$  is defined as follows:

$$C_D = F_D / qS, \quad (1)$$

where  $q = 1/2\rho U_{\infty}^2$  is the dynamic pressure and  $S = HW$  the frontal area of model. The statistical convergence of all cases discussed in the paper has been checked. The absolute error on the value of  $C_D$  is  $\pm 0.001$ .

### D. Measurements of base pressure and velocity

The base pressure is measured by 16 differential instantaneous pressure sensors (Sensortech-nics® HCLA02X5DB) distributed over the rear surface. Figure 1(d) presents the number and location of each pressure tap. The sensors have the following characteristics: operating pressure range is  $\pm 250$  Pa, response delay 0.5 ms, and uncertainty due to the nonlinearity and hysteresis less than 0.25% of full-scale span. The pressure measurements are sampled at a rate of 2.5 kHz. The dimensionless pressure coefficient is defined for each pressure tap  $i$  as

$$C_{p_i} = \frac{p_i - p_o}{q}, \quad i = 1, \dots, 16, \quad (2)$$

where  $p_i$  is the measured pressure and  $p_o$  the static pressure in the wind tunnel. In the following, the time- and area-averaged base pressure coefficients are denoted by  $\overline{C_p}$  and  $\langle C_p \rangle$ , respectively.

Particle image velocimetry (PIV) measurements are acquired in the lateral plane at mid height  $z = 0.67$ , as presented in Fig. 1(c). The measured region is illuminated by a laser sheet generated by a Nd:YAG laser. The entire wind tunnel is seeded by a fog generator (Antari X515) using Contest Hd liquid. Seeding droplets have a diameter of the order of  $1 \mu\text{m}$ . The images are captured by a LaVision Imager LX 16M camera with resolution of  $4920 \times 3280$  pixels. The time between a pair

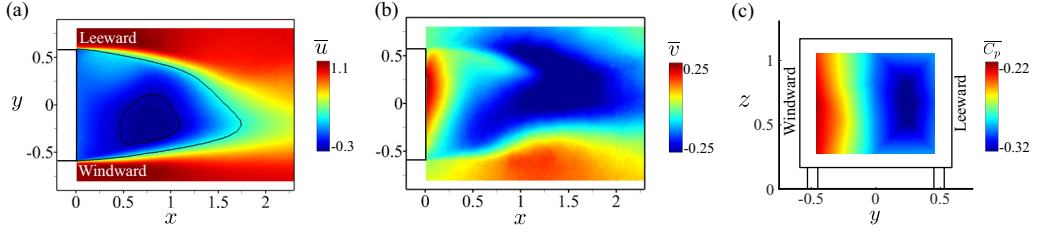


FIG. 3. Unforced flow. Mean wake in the mid-height plane  $z = 0.67$  and the mean base pressure. From (a) to (c): distribution of the mean streamwise velocity  $\bar{u}$ , the mean spanwise velocity  $\bar{v}$ , and the mean base pressure. Black lines in (a) are iso-contour lines at  $\bar{u} = \pm 0.25$ .

of images yielding one velocity field is  $50 \mu\text{s}$ . The image pairs are recorded at a sampling rate of 3.5 Hz. Velocity vectors are processed with an interrogation window of  $32 \times 32$  pixels with a 50% overlap, giving a spatial resolution of 2.7 mm corresponding to  $0.009H$ . The field of view covers a region of approximately  $2.5H \times 1.8H$ . The velocity statistics (mean velocities and Reynolds stresses) are computed with 1500 independent fields.

In what follows, all physical quantities are normalized by  $U_\infty$  and  $H$ . The frequencies are given in terms of  $\text{St}_H$ .

### III. UNFORCED FLOW AND FLUIDIC FLAP EFFECT AT HIGH-FREQUENCY FORCING

#### A. Unforced flow

In this section, we briefly introduce the unforced flow properties at yaw angle  $\beta = 5^\circ$ . The time-averaged velocity components in the mid-height plane  $z = 0.67$  and the mean base pressure distribution are presented in Fig. 3. All of them depict an asymmetric distribution. The iso-contour lines of the mean streamwise velocity  $\bar{u}$  in Fig. 3(a) are deviated towards the windward side, presenting a high curvature along the leeward side close to the end of the recirculation region. The distribution of  $\bar{v}$  in Fig. 3(b) shows that most of the free-stream flow is entrained into the wake region from the leeward side, as indicated by the large blue zone with negative  $\bar{v}$ . Thus, the mean wake exhibits a large clockwise recirculating motion on the leeward side as shown later in Fig. 5(a). Additionally, the distribution of  $\bar{C}_p$  in Fig. 3(c) is consistent with the velocity field. The large low-pressure zone close to the leeward edge shows the footprint of the large clockwise recirculating flow. This large recirculation curves the flow streamlines along the leeward bubble, thus generating high-pressure gradients associated with the decrease of pressure. The area- and time-averaged base pressure coefficient is  $\langle \bar{C}_p \rangle = -0.28$ . The associated mean drag coefficient is  $C_D = 0.274$ , about 3% higher than that of the aligned model. This increase is consistent with the results of [15]. To quantify further the degree of wake asymmetry, we calculate the time-averaged spanwise pressure gradient  $\partial \bar{C}_p / \partial y$ , where  $\partial \bar{C}_p / \partial y$  is defined as

$$\frac{\partial \bar{C}_p}{\partial y} = \frac{1}{2} \frac{C_{p8} - C_{p5}}{y_8 - y_5} + \frac{1}{2} \frac{C_{p7} - C_{p6}}{y_7 - y_6}. \quad (3)$$

The indices refer to the location of the pressure sensors in Fig. 1(d). For the unforced flow, we get  $\partial \bar{C}_p / \partial y = -0.11$ .

The wake dynamics can be inferred from the distribution of Reynolds stresses  $\overline{u'u'}$ ,  $\overline{v'v'}$ , and  $\overline{u'v'}$ , where  $u' = u - \bar{u}$  and  $v' = v - \bar{v}$  represent the velocity fluctuations. The results are shown in Fig. 4. All three quantities are prominent along the shear layers, especially for  $\overline{u'u'}$  and  $\overline{u'v'}$ , illustrating the important velocity fluctuations in these regions. Moreover, the windward shear layer features higher velocity fluctuations than those along the leeward shear layer, suggesting that the flow curvature on the leeward side has a stabilizing effect [31].

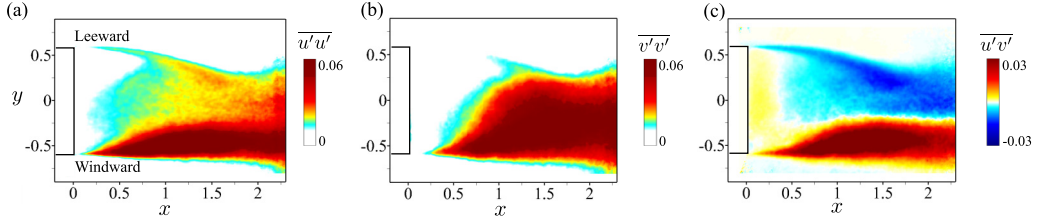


FIG. 4. Unforced flow. Distribution of Reynolds stresses in the mid-height plane  $z = 0.67$ . From (a) to (c):  $\overline{u'u'}$ ,  $\overline{v'v'}$ , and  $\overline{u'v'}$ .

It is noteworthy that the distributions of the velocity and Reynolds stresses in the horizontal mid-height plane  $z = 0.67$  for the yawed model are very similar to those on the vertical plane  $y = 0$  for the aligned model (see [18]) where the fluctuating motions are concentrated in the bottom shear layer with wall proximity. In particular, windward (leeward) shear layer resembles the bottom (top) shear layer of the aligned model. This observation suggests that the wake naturally selects one asymmetry depending on the operating condition [32], the locking of wake asymmetry being also reported for the axisymmetric geometry [33]. Furthermore, [34] shows that the asymmetry in the vertical plane of the aligned model can be induced and modified by upstream perturbations in the top and bottom boundary layers or by actuating the preferentially selected top/bottom shear layer with pulsed jets [35]. The present work aims to evaluate these strategies on the horizontal plane for the yawed model.

### B. Fluidic flap effect at $St_H = 6$

The use of high-frequency pulsed jets along the whole base periphery can create a fluidic *boat-tailing* effect characterized by an inward deviation of the shear layer immediately downstream of the separating edges and resulting in a thinner wake [18]. This effect is analogous to that of the inward-deviated flaps installed at the trailing edges studied for both aligned [36] and yawed car models [5]. The actuation frequency in this case is one order of magnitude higher than the natural wake vortex shedding mode. Building on these observations, we use the highest frequency permitted by the actuators ( $St_H = 6$ ,  $DC = 40\%$ ; see Table I) on the lateral trailing edges of the model. The aim is to create such fluidic flaps and to investigate their influence on drag. We note that  $St_H = 6 \approx 38 St_H^{vs}$ , where  $St_H^{vs} = 0.16$  is the natural vortex shedding frequency [18] measured in the wake of the aligned model. In the following, the drag variations due to actuation are quantified by the coefficient  $\gamma_D = C_{D_a}/C_{D_u}$ , where the subscript “u” represents the unforced flow and “a” stands for the actuated flow.  $\gamma_D < 1$  ( $\gamma_D > 1$ ) represents the drag reduction (increase).

We first study the application of  $St_H = 6$  on the windward edge. Figure 5 compares the unforced and the forced flows. The mean streamlines in Fig. 5(a) indicate that the high-frequency forcing does not change the organization of the mean recirculations. However, when looking at the iso-contour lines at  $\bar{u} \in \{-0.25, 0.25, 0.6\}$  in Fig. 5(b), they show clearly that the actuation leads to a bubble deviation towards the leeward side, suggesting the vectoring effect of the high-frequency forcing. To quantify this deviation, we compute the angle  $\theta = \arctan(\bar{v}/\bar{u})$  along the streamline emerging from the leeward and windward separation points  $(x, y) = (0, 0.6)$  and  $(x, y) = (0, -0.6)$ , respectively. The results are presented in Fig. 5(c). Along the leeward streamline, no deviation is noticed, while a higher angle is obtained all along the windward streamline. The angle at  $x = 0$  increases from  $2^\circ$  (unforced flow) to  $7.5^\circ$  (forced flow). In particular, the initial drop of  $\theta$  in the forced flow implies a sign reversal of streamline curvature immediately downstream of the forced edge, which is characteristic of a local rise in base pressure. This finding corroborates that forcing at  $St_H = 6$  is analogous to a fluidic flap that deviates the mean flow streamline at separation and modifies the base pressure. As a result, the base pressure is overall increased, as demonstrated in

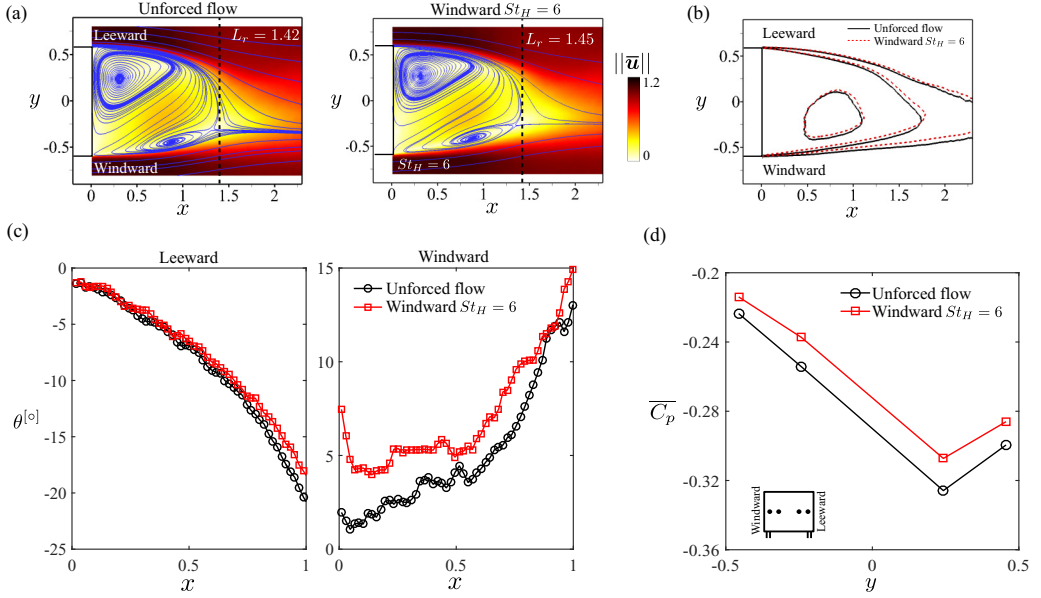


FIG. 5. Effect of the windward high-frequency forcing  $St_H = 6$  on the wake. (a) Streamlines of the mean velocity field overlapped with the contour maps of the velocity magnitude  $\|\bar{\mathbf{u}}\|$ . (b) Iso-contour lines of time-averaged streamwise velocity  $\bar{u} \in \{-0.25, 0.25, 0.6\}$ . Black line: unforced flow; red dashed line: high-frequency forced flow. (c) Streamwise evolution of the velocity angle  $\theta = \arctan(\bar{v}/\bar{u})$  of the streamline issuing from the leeward  $(x, y) = (0, 0.6)$  and windward separation point  $(x, y) = (0, -0.6)$ . (d)  $\bar{C}_p$  on the mid-height line.

Fig. 5(d) for the spanwise  $\bar{C}_p$  values. Note that the increase of  $\bar{C}_p$  is along the whole spanwise direction, yielding the same spanwise pressure gradient  $\partial \bar{C}_p / \partial y = -0.11$  as the unforced flow.

Additionally, for the windward forcing, we note from Fig. 5(a) a slight increase of the bubble length  $L_r$  of about 2%, where the bubble length  $L_r$  is defined as  $L_r = \max_x (\bar{u}(x, y, z) = 0)$ . A higher  $L_r$  is also reported in [18] and is related to the attenuation of the wake turbulent dynamics. We quantify this turbulence modification by integrating the turbulent kinetic energy  $\mathcal{K} = \overline{u'u'} + \overline{v'v'}$  inside the domain  $\Omega_{\bar{u} < 0}$  in the mid-height plane  $z = 0.67$ . The obtained integral value is reduced by 6% compared to that of the unforced flow. We conclude that the windward high-frequency forcing has not only a fluidic wake shaping effect like a deviated flap but also a stabilizing effect on the wake fluctuations.

In contrast, when applying  $St_H = 6$  along the leeward edge, the drag is increased by 4%. This result is consistent with that obtained in [5] for the inward-deviated leeward flap when the windward flap was maintained at  $0^\circ$ . As we focus in this paper on the drag reduction mechanisms, only the actuation along the windward edge is considered in the following.

#### IV. BI-FREQUENCY FORCING

For bimodal wakes, we observe a reduced drag when the wake locates at the transition states happening during the switch from one asymmetric state to the other [37–39]. One explanation is that the transition removes the presence of the low base pressure footprint induced by the asymmetric recirculation and related to high level of drag. Therefore, for intrinsic asymmetric wakes, targeting such unsteady symmetric wake could be another strategy of drag reduction. In [39], this mechanism was exploited to control a turbulent blunt body wake with pulsed jets via a closed-loop control approach. Based on the pressure feedback signal, each lateral trailing edge was

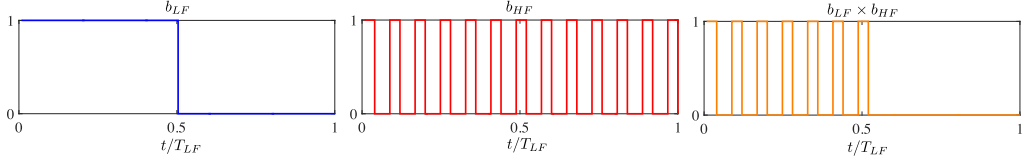


FIG. 6. Bi-frequency actuation command generated by the multiplication of two periodic square waves at low and high frequency respectively.  $T_{LF}$  corresponds to the period of the low-frequency component.

actuated intermittently at a predefined frequency. Their results showed that a range of low-frequency forcing is efficient to symmetrize the mean wake and thus to reduce the drag. In this study, the asymmetry of the near wake is induced by the yaw of the model. We then propose a bi-frequency forcing aiming to combine both high- and low-frequency forcing effects. By introducing lower frequencies in the actuation signal, the goal is to change the turbulent dynamics of the windward shear layer and to modify the dynamics of the slow recirculating bubble in the near wake. The interest of this strategy in terms of aerodynamic performance is evaluated by computing in Sec. IV C the actuation efficiency and relative power saving coefficients.

In what follows, we modulate the high-frequency actuation signal  $b_{HF}$  by the low-frequency actuation signal  $b_{LF}$ , as depicted in Fig. 6. The modulated signal is obtained by multiplying  $b_{HF}$  with  $b_{LF}$ . We note that the high-frequency period laying over  $t/T_{LF} = 0.5$  is enforced to be identical with its previous periods. The resulting forcing is denoted by  $St_{H_{bf}} = St_{H_{low}} \otimes St_{H_{high}}$ , where the subscript “bf” denotes bi-frequency. This kind of modulated actuation has been already investigated numerically by [40] on the development of a mixing layer and experimentally by [27] on a flat plate model.

#### A. Low frequency modulation

In this study, we fix the high frequency to  $St_{H_{high}} = 6$  with DC = 40% as studied in Sec. III B. However, a large range of low-frequency forcing can amplify the turbulent activity of the shear layer [18,39]. Hence, we perform a parametric study by varying the low frequency in the range  $St_{H_{low}} \in [0.12, 3]$  in order to determine the best actuation frequency in terms of the drag reduction. The duty cycle is about DC = 50% for all these low frequencies (see Table I).

To clarify the differences in the pulsed jet profile and actuation energy for single-frequency and bi-frequency forcings, we exemplify in Fig. 7(a) the phase-averaged jet velocity for  $St_H = 0.24$  and  $St_{H_{bf}} = 0.24 \otimes 6$  operating both at the constant supply pressure  $P_0 = 2.5$  bar. The velocity overshoot related to the sudden opening of the solenoid valve is about  $1.4U_\infty$  for both. This

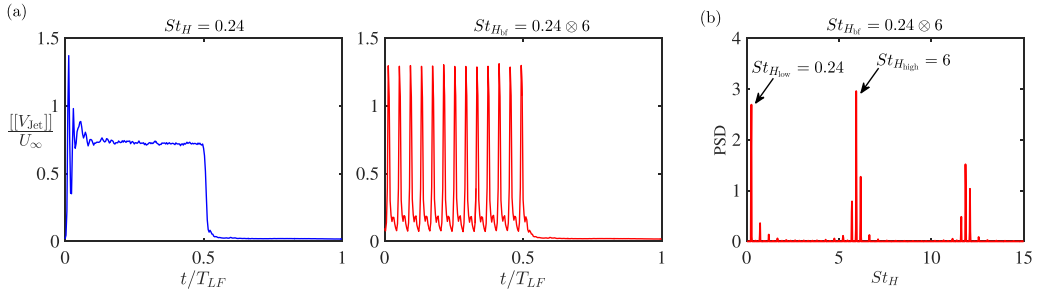


FIG. 7. (a) Phase-averaged jet velocity  $\llbracket V_{jet} \rrbracket / U_\infty$  for  $St_H = 0.24$  (left) and  $St_{H_{bf}} = 0.24 \otimes 6$  (right).  $T_{LF}$  is the period of the low-frequency forcing ( $St_H = 0.24$ ). (b) Power spectral density (PSD) of the jet velocity signal at  $St_{H_{bf}} = 0.24 \otimes 6$ .

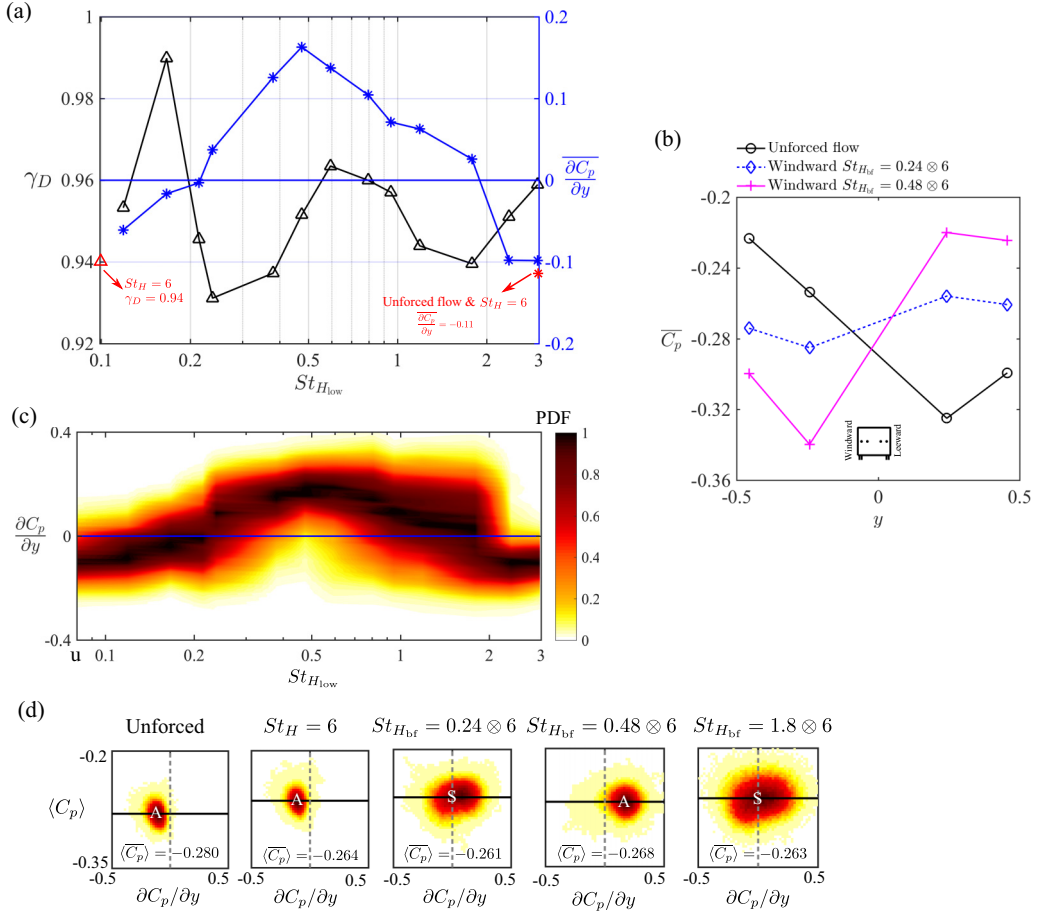


FIG. 8. Bi-frequency forcing results. (a) Variation of  $\gamma_D$  ( $\Delta$ ) and  $\overline{\partial C_p / \partial y}$  (\*) as a function of  $St_{H_{low}}$ . For comparison, the value  $\gamma_D = 0.94$  for  $St_H = 6$  is shown on the left y axis and the value  $\overline{\partial C_p / \partial y} = -0.11$  for both the unforced flow and  $St_H = 6$  is shown on the right y axis. (b)  $\overline{C_p}$  values on the mid-height line. (c) The evolution of PDF of  $\partial C_p / \partial y$  with increasing  $St_{H_{low}}$ . The PDFs are normalized by their maximum value. The letter “u” in the abscissa stands for the unforced flow. (d) The joint PDF of  $\langle C_p \rangle$  versus  $\partial C_p / \partial y$  for some highlighted configurations. The letters “A” and “S” indicate the asymmetric and symmetric state, respectively.

overshoot appears only once for  $St_H = 0.24$ , in contrast to its periodic occurrence for the case of  $St_{H_{bf}} = 0.24 \otimes 6$ . The velocity profile of high-frequency forcing in the latter case is similar to that of a single high-frequency forcing. The actuation energy at  $St_{H_{bf}} = 0.24 \otimes 6$  estimated from  $V_{eff}^2 = \overline{V_{jet}^2}$  is less than half that at  $St_H = 6$ . It is noteworthy that although two frequencies are given initially to the actuation command, the spectrum of the resulting jet is multifrequency, as shown in Fig. 7(b) for the spectrum of the jet velocity at  $St_{H_{bf}} = 0.24 \otimes 6$ . Clearly, the spectrum displays not only the two actuation frequencies but also their harmonics as well as their sums and differences.

Figure 8(a) presents the evolution of the drag ratio  $\gamma_D$  with increasing low-frequency  $St_{H_{low}}$ . For clarity, the abscissa is shown with a logarithmic scale. The performance of the high-frequency forcing at  $St_H = 6$  is reported for comparison on the left-hand ordinate axis. The highest drag reduction of about 7% is obtained at  $St_{H_{bf}} = 0.24 \otimes 6$ , outperforming the high-frequency forcing at  $St_H = 6$ . To shed light on the connection between the modification of the mean wake asymmetry and drag reduction, we present the time-averaged spanwise pressure gradient  $\partial C_p / \partial y$  in the same plot.

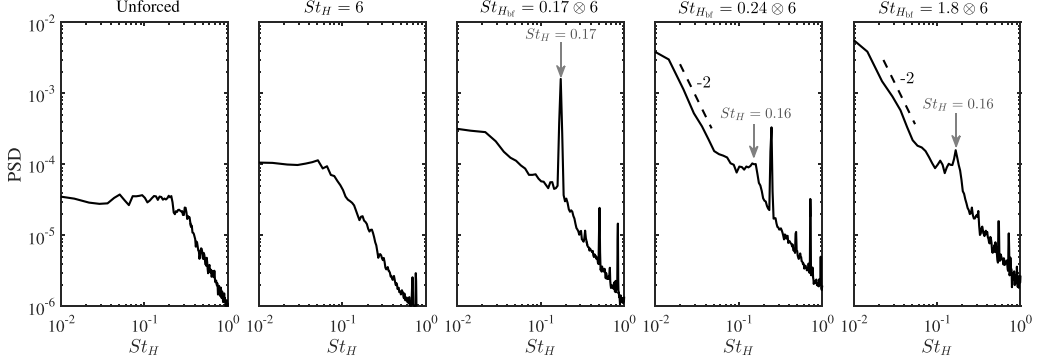


FIG. 9. Power spectral density (PSD) of the lateral pressure gradient  $\partial C_p / \partial y$  in the frequency range  $St_H = [0.01, 1]$ .

The value  $\overline{\partial C_p / \partial y} = -0.11$  for the unforced and the pure high-frequency forced flow ( $St_H = 6$ ) is also shown on the right-hand ordinate axis for comparison. The curve of  $\partial C_p / \partial y$  first increases up to a maximum positive value obtained at  $St_{H_{bf}} = 0.48 \otimes 6$ , and then decreases gradually to  $-0.1$  near the value of the unforced flow. It crosses the line of zero gradient two times. For  $\partial C_p / \partial y \approx 0$ , the mean wake is symmetrized by actuation. The interesting point is that the curve of  $\gamma_D$  shows a variation similar to that of  $\partial C_p / \partial y$  in the range  $St_{H_{low}} \in [0.24, 1.8]$  where the gradient is positive. In particular, the two actuations close to  $\partial C_p / \partial y = 0$ , namely  $St_{H_{bf}} = 0.24 \otimes 6$  and  $St_{H_{bf}} = 1.8 \otimes 6$ , correspond exactly to the global and local minimum observed in the curve of  $\gamma_D$ . This observation corroborates the correlation between the wake symmetrization and drag reduction. We further show in Fig. 8(b) the variation of the spanwise  $\overline{C_p}$  values for the forcing  $St_{H_{bf}} = 0.24 \otimes 6$ . Clearly, it leads to a more balanced distribution between the leeward and windward side. This nearly symmetric distribution is beneficial to attenuate the low pressure footprint (close to  $y = 0.24$ ) induced by the clockwise recirculating flow on the base. When  $\overline{\partial C_p / \partial y}$  reaches its maximum value at  $St_{H_{bf}} = 0.48 \otimes 6$ , the drag reduction performance degrades. This result corresponds to the reestablishment of the wake asymmetry. However, there is a reflectional change of the position of the lowest  $\overline{C_p}$ , as shown in Fig. 8(b), which points to a reversed wake asymmetry.

When  $St_{H_{low}} < 0.24$ , less drag reduction is achieved. In particular, at  $St_{H_{low}} = 0.17$  and  $0.21$ , a low drag reduction is obtained even if  $|\partial C_p / \partial y| \approx 0$ . The reason lies on the strong amplification of the oscillating vortex shedding when forcing at frequencies near the natural vortex shedding mode  $St_H^{vs} = 0.16$  (see Fig. 9) which has been shown to be detrimental to the drag reduction [20]. On the other hand, when increasing  $St_{H_{low}}$  over  $1.8$ , the value of  $\partial C_p / \partial y$  approaches to that of the unforced flow and the drag reduction performance degrades as well.

The results in Figs. 8(a) and 8(b) illustrate only the time-averaged variations by actuation. To infer the temporal changes of the wake, we show in Fig. 8(c) the evolution of the PDF (probability density function) of  $\partial C_p / \partial y$  as a function of  $St_{H_{low}}$ . The PDF of each case is normalized by its maximum value. The color indicates the level of PDF. Darker color means a higher PDF value. We see clearly that when the mean wake is symmetrized at  $St_{H_{bf}} = 0.24 \otimes 6$  and  $St_{H_{bf}} = 1.8 \otimes 6$ , their  $\partial C_p / \partial y$  show correspondingly a symmetric but highly fluctuating distribution. This indicates that the obtained symmetric states are highly unsteady, similar to the transition states in the bimodal wakes [38,39]. In addition, we are interested in how the temporal change of  $\partial C_p / \partial y$  influences the base pressure. For that, the joint PDF between the temporal area-averaged base pressure  $\langle C_p \rangle$  and the temporal signal of  $\partial C_p / \partial y$  is displayed in Fig. 8(d) for some highlighted configurations. For the case  $St_H = 6$ , although its joint PDF exhibits only one asymmetric state (indicated by the letter “A”) as the unforced flow, the corresponding  $\langle C_p \rangle$  values are overall increased. This finding is in agreement with the global increase of  $\overline{C_p}$  in Fig. 5(b) and demonstrates again that the fluidic flap

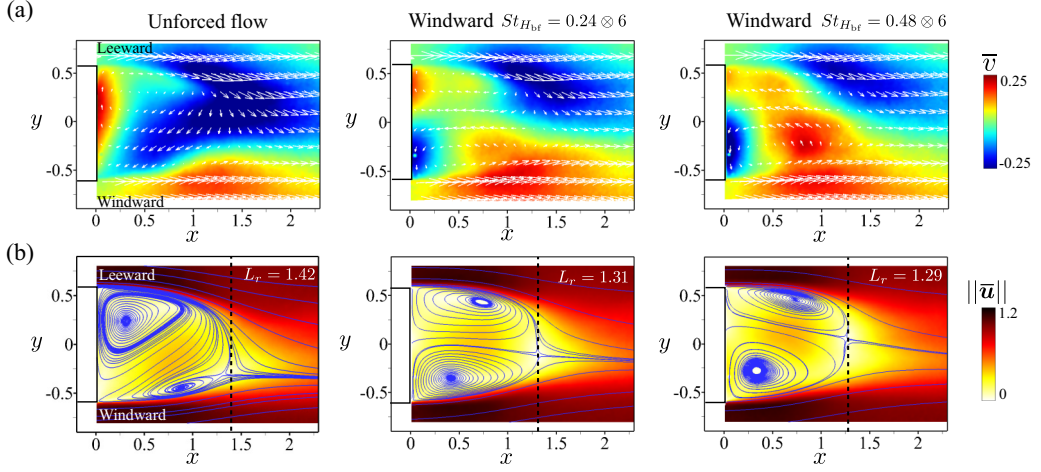


FIG. 10. Effects of bi-frequency actuation on the near wake. From left to right: unforced flow, windward forced flows at  $St_{H_{bf}} = 0.24 \otimes 6$  and  $St_{H_{bf}} = 0.48 \otimes 6$ . (a) Distributions of the time-averaged spanwise velocity  $\bar{v}$  on the mid-height plane  $z = 0.67$ . (b) Streamlines of the mean velocity field overlapped with the contour maps of the velocity magnitude  $\|\bar{\mathbf{u}}\| = \sqrt{\bar{u}^2 + \bar{v}^2}$ .

effect increases the base pressure without affecting the mean wake organization. At  $St_{H_{bf}} = 0.24 \otimes 6$  and  $St_{H_{bf}} = 1.8 \otimes 6$ , the PDF of  $\partial C_p / \partial y$  shows a symmetric distribution (indicated by the letter “S”). The values of  $\langle C_p \rangle$  are clearly increased at the S state when compared to the unforced flow and hence result in a higher time-averaged value  $\langle \bar{C}_p \rangle$ . However, the S state experiences a high fluctuation of  $\partial C_p / \partial y$ , clearly more fluctuating for  $St_{H_{bf}} = 1.8 \otimes 6$ . This may explain why the drag reduction achieved is less important at  $St_{H_{bf}} = 1.8 \otimes 6$ . At  $St_{H_{bf}} = 0.48 \otimes 6$ , a wake reversal occurs and the value  $\langle \bar{C}_p \rangle$  decreases.

Power spectral density (PSD) of  $\partial C_p / \partial y$  is also investigated to examine the frequency dynamics of the lateral wake. The results are shown in Fig. 9 for the unforced flow and four forced configurations. Among the forcing cases, when S states are observed in Fig. 8(c), an energy peak at the vortex shedding frequency  $St_H^{vs} = 0.16$  can be distinguished from their corresponding spectrum, i.e., for  $St_{H_{bf}} = 0.17 \otimes 6$ ,  $0.24 \otimes 6$ , and  $1.8 \otimes 6$ . In particular, this vortex shedding mode is significantly enhanced at  $St_{H_{bf}} = 0.17 \otimes 6$  because the actuation frequency is quite close to  $St_H^{vs} = 0.16$ . In addition, at  $St_{H_{bf}} = 0.24 \otimes 6$  and  $1.8 \otimes 6$ , we observe a slope of  $-2$  in the low-frequency range  $St_H < 0.1$ . This is a typical feature of the intermittent meandering of the large-scale asymmetric motions in the wake [37]. These findings suggest that, along with the wake symmetrization, the actuation concomitantly promotes the vortex shedding and gives rise to the low-frequency switching of wake asymmetry, both of them contributing to the high fluctuating behavior of the wake.

### B. Near wake reorganization under bi-frequency actuation

In the following, we focus on two forced configurations:  $St_{H_{bf}} = 0.24 \otimes 6$  and  $St_{H_{bf}} = 0.48 \otimes 6$ , which correspond to the minimum drag and the reversed wake asymmetry, respectively. The aim is to understand how the bi-frequency forcing interacts with the shear layer and modifies the wake properties. Figure 10 presents the time-averaged spanwise velocity  $\bar{v}$  (a) and the two-dimensional (2D) approximated streamlines in the mid-height plane  $z = 0.67$  (b) for the unforced and forced flows. The distribution of  $\bar{v}$  shows that the flow entrained into the wake from the windward side is clearly enhanced by actuation, while the entrainment from the leeward side is attenuated. For  $St_{H_{bf}} = 0.24 \otimes 6$  this enhancement results in a balanced mean wake with two counter-rotating mean

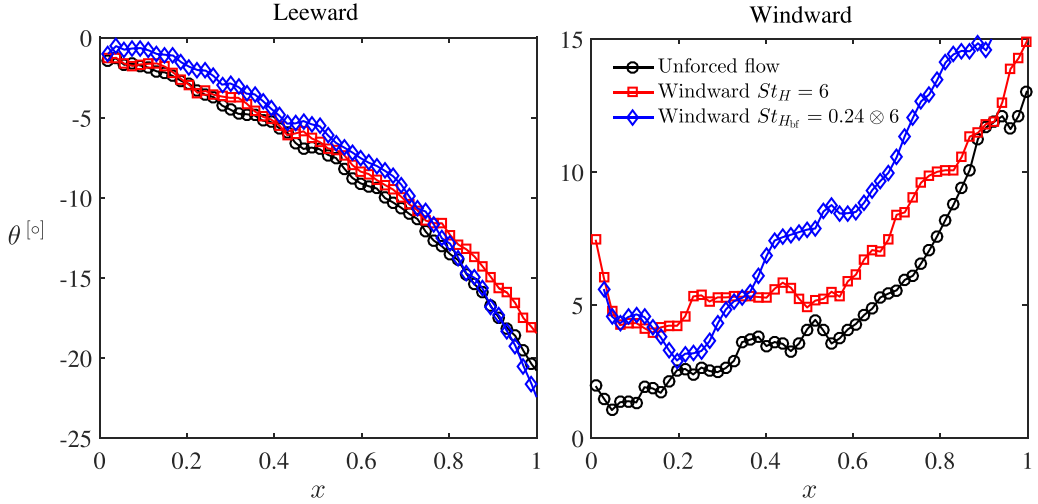


FIG. 11. Streamwise evolution of the velocity angle  $\theta = \arctan(\bar{v}/\bar{u})$  of the streamline issuing from the leeward  $(x, y) = (0, 0.6)$  and windward separation point  $(x, y) = (0, -0.6)$ .

recirculations of similar size, while for  $St_{H_{bf}} = 0.48 \otimes 6$  the entrainment is even stronger such that the positive  $\bar{v}$  crosses the central line  $y = 0$  and penetrates into the leeward side, hence reversing the wake asymmetry.

The change of wake organization is accompanied with a reduction of the bubble length [41]. Based on studies of 2D wakes [42], a shortened bubble with the conservation of the bubble height leads to a higher wake bluffness by reducing the aspect ratio  $L_r/H$ . The change of bluffness results in a lower radius  $R$  of the streamline curvature along the bubble boundary, decreasing the pressure inside the wake and near the model base. This is one reason why the single low-frequency forcing along the whole base periphery increases the drag of the aligned model [18]. However, in our study, the wake is symmetrized by applying solely the low-frequency component on the windward edge, and the fluidic flap effect related to  $St_{H_{high}} = 6$  still holds at  $St_{H_{bf}} = 0.24 \otimes 6$  as shown in Fig. 11. Similar to the case  $St_H = 6$  described in Sec. III B, an increase of  $\theta$  can be found immediately downstream of the trailing edge, pointing to the flow deviation by the fluidic flap effect. Further downstream ( $x > 0.4$ ),  $St_{H_{bf}} = 0.24 \otimes 6$  yields a higher value of  $\theta$  than  $St_H = 6$ , which is related to the change of the bubble curvature due to the wake symmetrization. A slight decrease of the absolute value of  $\theta$  is observed downstream the leeward trailing edge, indicating that the leeward curvature is also changed by the symmetrization. In summary, the mean wake at  $St_{H_{bf}} = 0.24 \otimes 6$  is not only symmetrized but also deviated, both contributing to the improvement of drag reduction.

The enhanced entrainment is closely related to the changes of the turbulent dynamics of the forced shear layer. Figure 12(a) compares the distribution of the Reynolds stress component  $\overline{u'v'}$  along the unforced and forced windward shear layer. Only the initial development of the shear layer in the range  $x \in [0, 0.5]$  is investigated. Both actuations,  $St_{H_{bf}} = 0.24 \otimes 6$  and  $St_{H_{bf}} = 0.48 \otimes 6$ , induce an increase of  $\overline{u'v'}$  immediately downstream of the trailing edge ( $x < 0.3$ ). This increase is particularly clear in Fig. 13 which presents the maximum value of  $\overline{u'v'}$  along the windward shear layer. Higher values of  $\overline{u'v'}$  indicate an enhancement of the transport of the fluctuating longitudinal momentum by the fluctuating lateral velocity. Consequently, the forced shear layer entrains more mass and momentum than the unforced shear layer in the near field  $x < 0.3$ . The low-frequency component enhances the coherent structures developing within the shear layer by introducing large-scale vortices originated from the pulsed jets [43]. The spatial correlation of the spanwise velocity

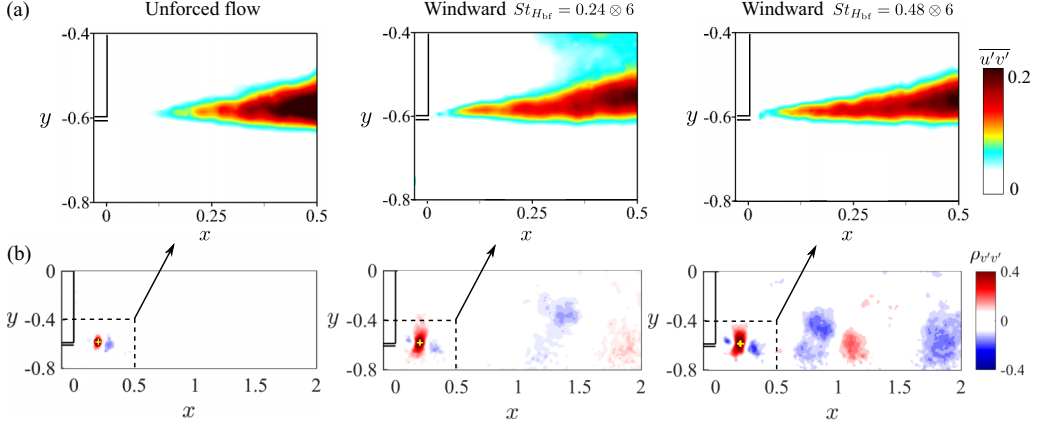


FIG. 12. Effects of bi-frequency actuation on the shear layers. From left to right: unforced flow,  $St_{H_{bf}} = 0.24 \otimes 6$ , and  $St_{H_{bf}} = 0.48 \otimes 6$ . (a) Distribution of  $\overline{u'v'}$  along the windward shear layer in the streamwise range  $x \in [0, 0.5]$ . (b) Distribution of the spatial correlation coefficient  $\rho_{v'v'}$  along the windward shear layer. The reference point  $(x_0, y_0)$  for each case is marked by “+” in the figure. At the reference point,  $\rho_{v'v'} = 1$ . The dashed line and arrow indicate the zone specified in (a).

fluctuation  $v'$  in the PIV plane is defined as

$$\rho_{v'v'}(x, y, x_0, y_0) = \frac{\overline{v'(x_0, y_0, t)v'(x, y, t)}}{\sigma_{v'}(x_0, y_0)\sigma_{v'}(x, y)}, \quad (4)$$

where  $\sigma_{v'}(x, y)$  denotes the standard deviation of  $v'$ .  $(x_0, y_0)$  is a reference point in the shear layer. We set  $x_0 = 0.2$ .  $y_0$  is then determined by the position of the vorticity extremum in the windward shear layer at  $x_0 = 0.2$ . The distributions of  $\rho_{v'v'}$  along the unforced and forced shear layers are shown in Fig. 12(b). The alternative negative and positive coefficients corroborate the existence of coherent structures which are responsible to bring high-momentum fluid into the recirculation region

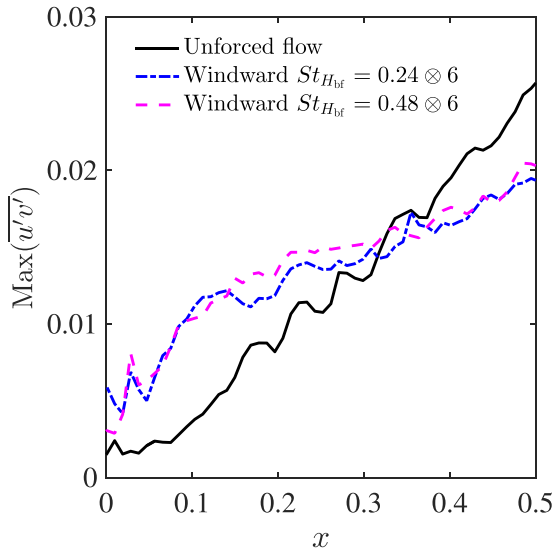


FIG. 13. Streamwise evolution of the maximum  $\overline{u'v'}$  along the windward shear layer.

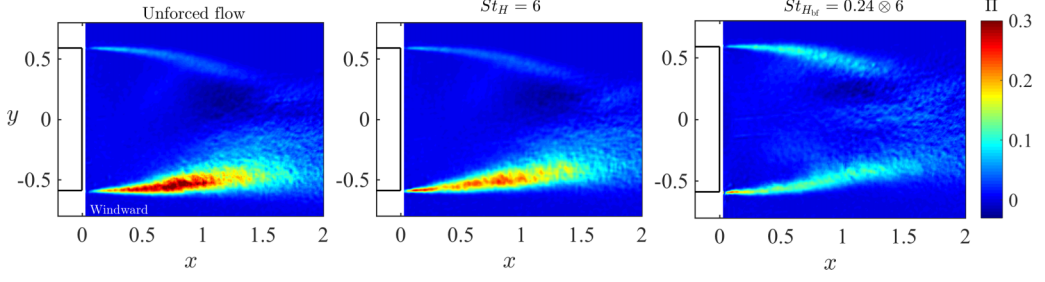


FIG. 14. Distribution of the production rate  $\Pi$  in the 2D plane  $(x, y) \in [0, 2] \times [-0.8, 0.8]$ .

and to transport low-momentum fluid out of the recirculation region. Two observations evidence the increase of coherent structures by both actuations. First, there is an increase of the coherence level in the field near the trailing edge. Second, the train of coherent structures extends downstream of the mean wake length  $L_r$ . The latter is particularly clear at  $St_{Hbf} = 0.48 \otimes 6$ .

Finally, we reconsider the actuation effects from the point of view of the energy balance. When looking into the balance of kinetic energy of the mean flow around the entire body, it can be shown that the power of the mean drag force just balances the viscous dissipation rate due to the mean shear and the production rate of turbulent kinetic energy in the entire flow. As the dissipation related to the mean shear is negligible in the wake flow, the dominant term of this balance is thus the production rate of turbulent kinetic energy, which is ultimately transformed into heat by the turbulent dissipation in the flow. Therefore, an estimation of the production term may help to understand the variation of drag force. For that, we calculate the integral of the production term in the whole wake domain for the unforced and forced flows. The integral  $\mathcal{P}$  is obtained by integrating the production rate  $\Pi$  in the 2D plane  $(x, y) \in [0, 2] \times [-0.8, 0.8]$ :

$$\mathcal{P} = \iint \underbrace{\left[ -\overline{u'u'} \frac{\partial \bar{u}}{\partial x} - \overline{v'v'} \frac{\partial \bar{v}}{\partial y} - \overline{u'v'} \left( \frac{\partial \bar{u}}{\partial y} + \frac{\partial \bar{v}}{\partial x} \right) \right]}_{\Pi(x,y)} dx dy. \quad (5)$$

Note that the 3D terms are missing. When normalizing the obtained  $\mathcal{P}$  by that of the unforced flow  $\mathcal{P}_u$ , we find 14% reduction for  $St_H = 6$  and 30% reduction for  $St_{Hbf} = 0.24 \otimes 6$ . Referring to Fig. 14 which shows the distribution of  $\Pi$  in the 2D plane, it is evident that this reduction is related to the change of the shear layer dynamics. For  $St_H = 6$  all of the 14% reduction comes from the decrease of  $\Pi$  along the windward shear layer, while for  $St_{Hbf} = 0.24 \otimes 6$  the 30% reduction is the superposition of two opposing effects as a consequence of the wake symmetrization: 50% decrease from the change of  $\Pi$  along the windward shear layer and 20% increase from the leeward shear layer. The balance between the windward and leeward shear layers has therefore an important role in minimizing the rate of kinetic energy transfer from the mean flow to turbulence.

### C. An estimation of the actuation energy input

As an energy input is required for the pulsed jets to achieve the control purpose, it is worth assessing the relation of the actuation energy input to the recovered energy obtained from the drag reduction. To quantify this relation, we define an actuation efficiency coefficient  $A_e$  and a relative power saving coefficient  $P_s$  as follows:

$$A_e = \frac{|\Delta C_D| S U_\infty^3}{S_{\text{Jet}} \overline{V_{\text{Jet}}^3}} \quad \text{and} \quad P_s = \frac{\frac{1}{2} |\Delta C_D| S U_\infty^3 - \frac{1}{2} S_{\text{Jet}} \overline{V_{\text{Jet}}^3}}{\frac{1}{2} C_{D_u} S U_\infty^3}, \quad (6)$$

where  $\Delta C_D = C_{D_u} - C_{D_a}$  and  $S_{\text{Jet}}$  is the jet slit area. Note that only the jet mechanical energy is considered here. The actuation efficiency  $A_e$  represents the ratio between the mechanical power

TABLE II. Synthesis of the actuation efficiency and relative power saving for drag reduction configurations.

| Configuration                               | $\gamma_D$ | $V_{\text{eff}}$ (m s <sup>-1</sup> ) | $C_\mu$ ( $\times 10^{-4}$ ) | $A_e$ | $P_s$ |
|---|------------|---------------------------------------|------------------------------|-------|-------|
| Windward ( $St_H = 6$ )                     | 0.94       | 13.6                                  | 8.5                          | 15    | 5.6%  |
| Windward ( $St_{H_{bf}} = 0.24 \otimes 6$ ) | 0.93       | 9.4                                   | 4.0                          | 44    | 6.7%  |

gained by the drag reduction and the mechanical power consumed by the pulsed jets. The relative power saving  $P_s$  represents the net power saving related to the control normalized by the power consumed by the aerodynamic drag in the unforced flow. Table II gives a summary of these quantities for  $St_H = 6$  and  $St_{H_{bf}} = 0.24 \otimes 6$ . The effective jet velocity  $V_{\text{eff}}$  and the momentum coefficient  $C_\mu = S_{\text{jet}} V_{\text{eff}}^2 / S U_\infty^2$  are also shown for comparison of the actuation amplitude. Both values of  $A_e$  are greater than 1 and both values of  $P_s$  are greater than 0, indicating that the net energy balance is positive. At  $St_{H_{bf}} = 0.24 \otimes 6$ , the actuation efficiency  $A_e$  is almost tripled compared to that at  $St_H = 6$ . Hence, the actuation with frequency modulation appears to be a promising strategy for further applications on bluff body drag reduction control.

## V. CONCLUSION

We manipulated experimentally the wake past a square-back car model at a moderate yaw angle of  $5^\circ$  using pulsed jets along the lateral trailing edges. The focus was placed on the windward forcing as leeward forcing leads to drag increase [29]. The drag reduction mechanisms related to the windward forcing are sketched in Fig. 15. High-frequency forcing ( $St_H = 6$  in the present study) acts as a time-invariant flap compared to the timescale of the large-scale structures within the shear layer [19]. This fluidic flap effect deviates the windward shear layer towards the leeward side, changing the streamline curvature downstream of the trailing edge and narrowing the mean wake. As a consequence, the mean base pressure is globally increased along the whole spanwise direction. Moreover, the actuation decreases the turbulent kinetic energy in the wake and leads to an increase

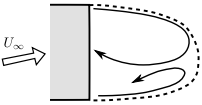
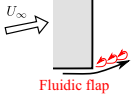
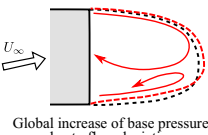
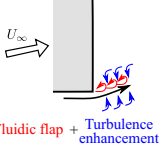
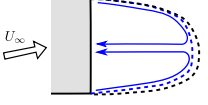
| Forcing   | Drag reduction mechanism  | Drag reduction | Actuation efficiency $A_e$ | In-plane production reduction |
|---|---|----------------|----------------------------|-------------------------------|
| No forcing  |    |                |                            |                               |
| Windward HF<br>    | <br>Global increase of base pressure due to flow deviation | 6%             | 15                         | 14%                           |
| Windward HF+LF<br> | <br>Flow deviation + Wake symmetrization                   | 7%             | 44                         | 30%                           |

FIG. 15. Synthesis of drag reduction performances and mechanisms. The inserted sketches illustrate qualitatively the recirculating flow in the wake. HF and LF represent high frequency and low frequency respectively.

of the bubble length. Hence, the high-frequency forcing leads to a lower wake bluffness which also contributes to drag reduction [42]. The drag reduction related to this high-frequency forcing is about 6%.

We exploit recent works showing that, for intrinsic bimodal wake, the slow unsteady transition from one state to another corresponds to a lower drag. Therefore, we proposed a bi-frequency actuation by modulating the high-frequency signal ( $St_H = 6$ ) with a low-frequency signal. It was shown that, by varying the low frequency value while maintaining the fluidic flap effect, we can “tune” the turbulence forcing to provide a complete authority for the manipulation of mean wake orientation. Once the forcing promotes a statistical mean symmetric wake, we achieve a global benefit on drag. At  $St_{bf} = 0.24 \otimes 6$ , the benefit reaches 7%. The mean wake in this case is simultaneously thinned and symmetrized. The drag reduction mechanism lies not only on the wake deviation but also on the wake symmetrization, which attenuates the low pressure footprint on the base induced by the large-scale asymmetric organized recirculation. We also showed that the balance between the windward and leeward shear layers has an important role in minimizing the rate of kinetic energy transfer from the mean flow to turbulence. Even if  $St_{bf} = 0.24 \otimes 6$  results in only 1% additional drag reduction compared to  $St_H = 6$ , it exhibits a large benefit on the actuation energy by tripling the actuation efficiency.

Additionally, *linear genetic programming control* (LGPC) [30], an automatic control optimization method using machine learning, was used in order to make a systematic study of the optimal multifrequency forcing applied to the windward trailing edge (for details, see [29]). This study confirmed that the combination of the two frequencies  $St_H = 0.24$  and  $St_H = 6$  outperforms the other configurations examined automatically. Note that this result is achieved without any prior knowledge about the control system and the underlying physics. However, with the analyses in the present paper, it is clarified that this control reduces the drag by targeting two different physical mechanisms (lower wake bluffness and wake symmetrization) in the near wake control.

The coupling of low- and high-frequency actuation mechanisms proposed in our study opens a new path for the control of wakes and fluid forces. It shows that both (fluidic) flap effect and turbulence control effect can be used and combined to achieve a drag reduction. In fact, the formation of mean asymmetric recirculation regions is a classical feature of near wake flows, not only for yawed situations ([33], present work) but also for perfectly aligned bodies [34,37,44]. These asymmetric recirculations are detrimental to the drag as they induce a low pressure footprint on the base. However, the buildup of these large-scale motions in the near wake is a slow process (see, e.g., [39]). We believe that one essential merit of the control strategy used here is to prevent the formation of these steady (quasisteady for bimodal wakes) asymmetric recirculations in the near wake flow. An ongoing study is to apply this low-frequency modulation on the configuration having 22% drag reduction by the high-frequency Coandă blowing along all four trailing edges [30]. The modulation would enable maintaining simultaneously the mean wake symmetry and the fluidic boat tail and may thus lead to further drag reduction. More generally, it may provide robust control of the high-frequency Coandă blowing for various attitudes (pitch and/or yaw) of the model or even various upstream perturbations on the surface of the model [34] by applying the modulation along the relevant trailing edge. For more complex situations like gust, the wake asymmetry depends on the variable yaw angle. In these cases, a closed-loop control [45] of the mean wake symmetry, using both horizontal and vertical pressure gradient information, may be a useful strategy to reduce the drag of vehicles. This would be the future direction of the current research.

## ACKNOWLEDGMENTS

We warmly thank the great support during the experiment by J.-M. Breux, F. Paillé, J. Laumonier, P. Braud and R. Bellanger. The work of R.L. is supported by the PSA Groupe in the context of OpenLab Fluidics (Fluidics@Poitiers). This work is also supported by a public grant overseen by the French National Research Agency (ANR) as part of the “Investissement d’Avenir” program, through the “iCODE Institute project” funded by the IDEX Paris-Saclay, ANR-11-IDEX-0003-02, and by

the ANR grants ANR-15-CE22-0002 (ACTIV\_ROAD) and ANR-17-ASTR-0022 (FlowCon). We appreciate valuable stimulating discussions with Diogo Barros and Andreas Spohn.

---

- [1] C. Baker, *J. Wind Eng. Ind. Aerodyn.* **22**, 69 (1986).
- [2] M. Gohlke, J.-F. Beaudoin, M. Amielh, and F. Anselmet, *Exp. Fluids* **43**, 579 (2007).
- [3] C. N. Nayeri, D. Wieser, H. J. Schmidt, C. Strangfeld, and O. Paschereit, in *The International Vehicle Aerodynamics Conference* (Woodhead, Sawston, UK, 2014), p. 43.
- [4] M. Grandemange, O. Cadot, A. Courbois, V. Herbert, D. Ricot, T. Ruiz, and R. Vigneron, *J. Wind Eng. Ind. Aerodyn.* **145**, 282 (2015).
- [5] J. M. García de la Cruz, R. Brackston, and J. Morrison, Adaptive Base-Flaps Under Variable Cross-Wind, SAE Technical Paper, No. 2017-01-7000 (2017).
- [6] G. Rossitto, C. Sicot, V. Ferrand, J. Borée, and F. Harambat, *Proc. Inst. Mech. Eng. Part D: J. Automobile Eng.* **231**, 9 (2017).
- [7] A. D’Hooge, R. Palin, L. Rebbeck, J. Gargoloff, and B. Duncan, *SAE Int. J. Passeng. Cars-Mech. Syst.* **7**, 617 (2014).
- [8] J. Howell, *SAE Int. J. Passeng. Cars-Mech. Syst.* **8**, 306 (2015).
- [9] J. Kim and T. R. Bewley, *Annu. Rev. Fluid Mech.* **39**, 383 (2007).
- [10] H. Choi, W.-P. Jeon, and J. Kim, *Annu. Rev. Fluid Mech.* **40**, 113 (2008).
- [11] C. Nayeri, J. Haff, D. Greenblatt, L. Loefdahl, and C. Paschereit, in *The Aerodynamics of Heavy Vehicles II: Trucks, Buses, and Trains* (Springer, Berlin, 2009), pp. 179–191.
- [12] R. Littlewood and M. Passmore, *Exp. Fluids* **53**, 519 (2012).
- [13] M. Grandemange, A. Mary, M. Gohlke, and O. Cadot, *Exp. Fluids* **54**, 1529 (2013).
- [14] H. Schmidt, R. Woszidlo, C. Nayeri, and C. Paschereit, *Exp. Fluids* **56**, 151 (2015).
- [15] J. Pfeiffer and R. King, in *6th AIAA Flow Control Conference, Atlanta, 2012* (AAIA, Washington, DC, 2012), pp. 1–14.
- [16] J. Pfeiffer and R. King, *Exp. Fluids* **59**, 45 (2018).
- [17] L. Cattafesta and M. Shelpak, *Annu. Rev. Fluid Mech.* **43**, 247 (2011).
- [18] D. Barros, J. Borée, B. R. Noack, A. Spohn, and T. Ruiz, *J. Fluid Mech.* **805**, 422 (2016).
- [19] A. Glezer, M. Amitay, and A. Honohan, *AIAA J.* **43**, 1501 (2005).
- [20] D. Barros, J. Borée, B. R. Noack, and A. Spohn, *Phys. Fluids* **28**, 065104 (2016).
- [21] N. Gao, Y. Q. Li, H. L. Bai, and C. J. Wu, *Flow Turbul. Combust.* **97**, 729 (2016).
- [22] M. Pastoor, L. Henning, B. R. Noack, R. King, and G. Tadmor, *J. Fluid Mech.* **608**, 161 (2008).
- [23] J. F. Morrison and A. Qubain, *Adv. Turbul.* **XII**, 225 (2009).
- [24] B. Vukasinovic, Z. Rusak, and A. Glezer, *J. Fluid Mech.* **656**, 51 (2010).
- [25] A. Oxlade, J. Morrison, A. Qubain, and G. Rigas, *J. Fluid Mech.* **770**, 305 (2015).
- [26] G. Minelli, S. Krajnović, and B. Basara, *J. Fluids. Eng.* **140**, 121101 (2018).
- [27] J. C. Griffin, M. Oyarzun, L. N. Cattafesta, J. H. Tu, and C. W. Rowley, in *43rd AIAA Fluid Dynamics Conference, San Diego, June 2013* (AAIA, Washington, DC, 2013), pp. 1–19.
- [28] S. Ahmed, G. Ramm, and G. Faltin, SAE Technical Paper 840300 (1984), <https://doi.org/10.4271/840300>.
- [29] R. Li, Aerodynamic drag reduction of a square-back car model using linear genetic programming and physics-based control, Ph.D. thesis, École Nationale Supérieure de Mécanique et d’Aérotechnique, Poitiers, France, 2017.
- [30] R. Li, B. R. Noack, L. Cordier, J. Borée, and F. Harambat, *Exp. Fluids* **58**, 1 (2017).
- [31] P. Bradshaw, Effects of Streamline Curvature on Turbulent Flow, Technical Report, Advisory Group for Aerospace Research and Development, Paris, 1973.
- [32] G. Bonnavion and O. Cadot, *J. Fluid Mech.* **854**, 196 (2018).
- [33] V. Gentile, B. W. van Oudheusden, F. F. J. Schrijer, and F. Scarano, *J. Fluid Mech.* **813**, R3 (2017).
- [34] D. Barros, J. Borée, O. Cadot, A. Spohn, and B. R. Noack, *J. Fluid Mech.* **829**, R1 (2017).

- [35] D. Barros, J. Borée, A. Spohn, and B. R. Noack, in *10th International Symposium On Turbulent and Shear Flow Phenomena (TSFP-10)*, Chicago (2017), pp. 1–5.
- [36] B. Khalighi, K. H. Chen, and G. Iaccarino, *J. Fluids Eng.* **134**, 061101 (2012).
- [37] M. Grandemange, M. Gohlke, and O. Cadot, *J. Fluid Mech.* **722**, 51 (2013).
- [38] R. D. Brackston, J. M. García de la Cruz, A. Wynn, G. Rigas, and J. F. Morrison, *J. Fluid Mech.* **802**, 726 (2016).
- [39] R. Li, D. Barros, J. Borée, O. Cadot, B. R. Noack, and L. Cordier, *Exp. Fluids* **57**, 158 (2016).
- [40] O. Inoue, *J. Fluid Mech.* **234**, 553 (1992).
- [41] J. H. Gerrard, *J. Fluid Mech.* **25**, 401 (1966).
- [42] A. Roshko, *J. Aeronaut. Sciences* **22**, 124 (1955).
- [43] T. Berk, T. Medjnoun, and B. Ganapathisubramani, *Phys. Rev. Fluids* **2**, 074605 (2017).
- [44] G. Rigas, A. R. Oxlade, A. S. Morgans, and J. F. Morrison, *J. Fluid Mech.* **755**, R5 (2014).
- [45] S. L. Brunton and B. R. Noack, *Appl. Mech. Rev.* **67**, 050801 (2015).